



LAWRENCE
LIVERMORE
NATIONAL
LABORATORY

Seismoelectric Phenomena in Fluid-Saturated Sediments

G. I. Block, J. G. Harris

April 25, 2005

Journal of Geophysical Research

Disclaimer

This document was prepared as an account of work sponsored by an agency of the United States Government. Neither the United States Government nor the University of California nor any of their employees, makes any warranty, express or implied, or assumes any legal liability or responsibility for the accuracy, completeness, or usefulness of any information, apparatus, product, or process disclosed, or represents that its use would not infringe privately owned rights. Reference herein to any specific commercial product, process, or service by trade name, trademark, manufacturer, or otherwise, does not necessarily constitute or imply its endorsement, recommendation, or favoring by the United States Government or the University of California. The views and opinions of authors expressed herein do not necessarily state or reflect those of the United States Government or the University of California, and shall not be used for advertising or product endorsement purposes.

Seismoelectric Phenomena in Fluid-Saturated Sediments

Gareth I. Block

Lawrence Livermore National Laboratory

7000 East Avenue, L-206, Livermore, CA 94566

block4@llnl.gov, 925-423-8547

John G. Harris

Ctr. QEEP, Northwestern University

2137 N. Sheridan Rd., Evanston, IL 60208-3020

Abstract: Seismoelectric phenomena in sediments arise from acoustic wave-induced fluid motion in the pore space, which perturbs the electrostatic equilibrium of the electric double layer on the grain surfaces. Experimental techniques and the apparatus built to study this electrokinetic (EK) effect are described and outcomes for studies of seismoelectric phenomena in loose glass microspheres and medium-grain sand are presented. By varying the NaCl concentration in the pore fluid, we measured the conductivity dependence of two kinds of EK behavior: (1) the electric fields generated within the samples by the passage of transmitted acoustic waves, and (2) the electromagnetic wave produced at the fluid-sediment interface by the incident acoustic wave. Both phenomena are caused by relative fluid motion in the sediment pores—this feature is characteristic of poroelastic (Biot) media, but not predicted by either viscoelastic fluid or solid models. A model of plane-wave reflection from a fluid-sediment interface using EK-Biot theory leads to theoretical predictions that compare well to the experimental data for both sand and glass microspheres.

1 Introduction

We developed electrokinetic techniques in the laboratory to monitor acoustic wave propagation in electrolyte-saturated, unconsolidated sediments. Because most underwater imaging and naval operations require predicting the acoustical properties of the seabed, one application of our work is to the question: Are ocean seabed sediments best described by viscoelastic fluid or solid models, or poroelastic ones? Experimentally derived, ad hoc viscoelastic fluid and solid models commonly used in ocean acoustics [*Hamilton*, 1972, 1974] are often unable to predict how frequency-dependent behavior varies with sediment type because they lack a direct connection between micro- and macroscale properties. To remedy this situation, a number of researchers (e.g., *Stoll* [1983, 2002], *Chotiros* [1995], *Williams* [2001], and *Williams et al.* [2002]) have studied models based on the Biot theory of poroelasticity [*Biot*, 1956a, 1956b]. And extensions have been made to these models to account for grain contact [*Biot*, 1962; *Tutuncu and Sharma*, 1992], stick-slip phenomena [*Buckingham*, 1997, 1998, 2005], and “squirt flow” [*Murphy et al.*, 1986; *Dvorkin and Nur*, 1993; *Chotiros and Isakson*, 2004]. While traditional acoustical methods have had difficulty distinguishing experimentally among the predictions of these competing theories, only poroelastic media are capable of generating a macroscopic, EK response. Techniques that measure seismoelectric phenomena offer a unique means of assessing how successfully Biot theory (and its extensions) model sediments.

The coupled EK-Biot theory developed by *Pride* [1994] describes how acoustic waves generate electromagnetic (EM) waves (the seismoelectric effect), and reciprocally, how electromagnetic fields generate acoustic waves (the electroseismic effect) in electrolyte-saturated, porous media. Both seismoelectric and electroseismic imaging

techniques have been developed for field research [*Thompson and Gist*, 1991; *Mikhailov et al.*, 1997; *Zhu et al.*, 1999], well-logging [*Chandler*, 1981], and modeled numerically [*Haartsen and Toksöz*, 1996; *Pride and Haartsen*, 1996; *Haartsen and Pride*, 1997]; *Beamish* [1999] provides a good review of these techniques in seismology. In the context of material characterization, a simplified form of EK-Biot theory was used to study the permeability and pore features of consolidated rock and sandstones at frequencies below 100 Hz [*Pengra and Wong*, 1995; *Pengra et al.*, 1999], and constant flow-rate EK measurements have been performed in unconsolidated sand [*Ahmed*, 1964].

We measured high-frequency (10 – 800 kHz) seismoelectric potentials in laboratory experiments using unconsolidated medium-grain sand and loose glass microspheres, which were saturated by NaCl electrolytes with a range of electrical conductivities. In the following sections we describe these measurements and compare them to predictions derived from coupled EK-Biot theory. Section 2 introduces EK phenomena and the coupled EK-Biot theory. The apparatus and typical data sets in medium-grain sand and loose glass microspheres are described in Section 3. In Section 4, we derive expressions for plane-wave reflection and transmission from a fluid-sediment interface to analyze how seismoelectric-wave phenomena depend on frequency, angle of incidence, and pore-fluid conductivity. We compare our experimental results with the predictions of the EK-Biot theory in Section 5. Section 6 summarizes and concludes with a discussion of the impact of EK measurement techniques in sediment acoustics. Material properties and analyses of the samples tested are given in Appendices A and B, respectively.

2 Electrokinetics

2.1 Electric Double Layer

Electrokinetic phenomena arise because an electric double layer forms near the grain surface, as shown in Figure 1. The bare surface of silicon dioxide (SiO^- , the prime constituent of glass and sand) often carries a small negative charge due to naturally deprotonated silanol groups (Si-O_2). When in contact with an electrolyte—say, NaCl in water—this surface charge creates an electric potential that affects the charge distribution in the surrounding fluid. A physical model for this structure was developed by *Gouy* [1910], *Debye and Huckel* [1923], and *Stern* [1924] who developed the “double layer” concept. In the simplest case, counter ions (Na^+) in the pore fluid are attracted to and adsorbed by the negatively charged grains; they are bound chemically in an atomically thin, immobile layer. Further from the surface is a distribution of mobile counter ions in a diffuse layer [*Hiemenz and Rajagopalan*, 1997]. The potential at the interface between the immobile and diffuse layers is called the ζ potential. It is sensitive to the available binding sites at the grain surface, as well as to the electrolyte concentration and pH of the pore fluid. Because the electric potential decays exponentially away from the grain wall, the effective thickness of the electric double layer is often less than 10 nm.

A simple example of EK phenomena arises in the case of fluid flow in a silica capillary [*Rice and Whitehead*, 1965]. An electric field aligned parallel to the grain wall causes the ions in the diffuse layer to move, dragging the pore fluid along with it because of the presence of viscous stresses. The reciprocal effect also exists: an applied pressure gradient will create both fluid flow and ionic convection current, which in turn, produces

an electric potential. To study these phenomena in poroelasticity at a macroscopic scale, the average acoustic and electromagnetic fields in the presence of a complex network of capillaries must be determined. Previous models of seismoelectric phenomena in geophysics [*Frenkel*, 1944; *Fitterman*, 1978; *Auriault and Strzelecki*, 1981; *Neev and Yeats*, 1989] and colloidal chemistry [*O'Brien*, 1988] did not use the full set of Maxwell's equations and/or limited their scope to the low-frequency case. They therefore failed to predict key theoretical and experimental behaviors—such as EM-wave generation at a fluid-sediment interface caused by a high-frequency, incident acoustic wave—that are a robust feature in our experimental data. It is for this reason that we use the full coupled EK-Biot theory.

2.2 Coupled Electrokinetic-Biot Theory

Poroelasticity depends (often implicitly) on the notion of a hierarchy of scales. Transducers fix the scale of our observations. Consider, for example: (1) the size of their active surfaces, which form a portion of the macroscopic boundary, (2) their frequency response and bandwidth, which together define a range of resolvable time scales, and (3) the strength of their interactions with the material, which determines just how far from equilibrium the material will be driven. We focus on small amplitude disturbances with operating frequencies less than 1 MHz, so that the acoustic wavelength is always much larger than typical grain-scale heterogeneities. The sediments are also assumed to be homogeneous and isotropic on the macroscale in what follows.

Because poroelasticity depends on the kinematics of both the fluid and solid, it requires two macroscale balance laws. To derive these laws, *Pride* [1994] applied the

techniques of volume averaging [Slattery, 1967] to locally average the microscale acoustic and electromagnetic field equations. Coupling along the interfaces between the fluid and solid phases results in nontrivial (and often frequency-dependent) poroelastic coefficients. The first law describes the balance of linear momentum:

$$-\omega^2 (\rho_{bulk} \bar{\mathbf{u}}_s + \rho_f \bar{\mathbf{w}}) = \nabla \cdot \boldsymbol{\tau}_{bulk}. \quad (1)$$

The second law describes macroscale fluid flow; it is a form of Darcy's law, which we give shortly. A time dependence of $\exp(-i\omega t)$, with angular frequency ω , is assumed, and overbars denote locally averaged quantities. Here,

$$\begin{aligned} \boldsymbol{\tau}_{bulk} &= (1 - \phi) \bar{\boldsymbol{\tau}}_s - \phi \bar{p} \mathbf{I} \\ \rho_{bulk} &= (1 - \phi) \rho_{bulk} + \phi \rho_f \\ \bar{\mathbf{w}} &= \phi (\bar{\mathbf{u}}_f - \bar{\mathbf{u}}_s). \end{aligned} \quad (2)$$

The variables $\bar{\mathbf{u}}_s$, $\bar{\mathbf{u}}_f$, $\bar{\mathbf{w}}$, \bar{p} , and $\bar{\boldsymbol{\tau}}_s$ are the average fluid displacement, solid displacement, relative fluid displacement, fluid pressure, and solid stress tensor, respectively. The fluid density ρ_f and solid density ρ_s combine to form a bulk density ρ_{bulk} based on the fluid volume fraction ϕ . Constitutive relations are given in (A.1) – (A.3) in Appendix A.

Volume-averaged versions of Maxwell's equations are also determined for the porous medium:

$$\begin{aligned} \nabla \times \bar{\mathbf{E}} &= i\omega \mu_0 \bar{\mathbf{H}} \\ \nabla \times \bar{\mathbf{H}} &= -i\omega \epsilon_{bulk} \bar{\mathbf{E}} + \bar{\mathbf{J}}. \end{aligned} \quad (3)$$

Here, $\bar{\mathbf{E}}$ and $\bar{\mathbf{H}}$ are the average electric and magnetic fields and $\bar{\mathbf{J}}$ is the average current density. The magnetic permeability μ_0 is assumed constant for both the fluid and solid.

The bulk permittivity of the porous medium,

$$\varepsilon_{bulk} = \varepsilon_0 \left[\frac{\phi}{\alpha_\infty} (\kappa_f - \kappa_s) + \kappa_s \right], \quad (4)$$

is defined in terms of the porosity ϕ , sediment tortuosity α_∞ , vacuum permittivity ε_0 , and dielectric constants for the fluid and solid phases, κ_f and κ_s , respectively.

The primary result of averaging is that Darcy's and Ohm's laws are coupled when the presence of the electric double layer is taken into account. Following *Pride* [1994], these flux-force relations can be written in a symmetric form:

$$\begin{aligned} -i\omega \bar{\mathbf{w}} &= \frac{k(\omega)}{\eta} (-\nabla \bar{p} + \rho_f \omega^2 \bar{\mathbf{u}}_s) + L(\omega) \bar{\mathbf{E}} \\ \bar{\mathbf{J}} &= L(\omega) (-\nabla \bar{p} + \rho_f \omega^2 \bar{\mathbf{u}}_s) + \sigma_{bulk}(\omega) \bar{\mathbf{E}}. \end{aligned} \quad (5)$$

The first line in (5) is an augmented form of Darcy's law based on the viscosity of the fluid η and dynamic permeability $k(\omega)$ (defined in (A.4) – (A.6)), which captures the effect of sound-speed dispersion and attenuation in sediments by modeling the transition from viscous pore flow at low frequencies to a type of boundary-layer flow near the grain surfaces at high frequencies [*Pride et al.*, 1992].

The electrokinetic-coupling coefficient $L(\omega)$ (defined in (A.7) – (A.9)) depends explicitly on the electric double-layer properties. When $L(\omega)$ is set to zero, Darcy's and Ohm's laws are uncoupled and we obtain the original Biot theory and Maxwell's equations. The second line of (5) is a generalization of Ohm's law: it consists of contributions from bulk electromigration and ionic convection currents generated by fluid flow in the pore space. The bulk electrical conductivity $\sigma_{bulk}(\omega)$ plays an important role in EK-Biot theory and is discussed at length in Section 3.3.

3 Laboratory Experiment

3.1 Apparatus

A diagram of our apparatus is given in Figure 2. Seismoelectric phenomena are excited by an acoustic, sine-wave burst injected at the top of the apparatus; this wave propagates down the fluid-filled tube and impacts the saturated sediment about 750 μs later. The incident wave generates reflected and transmitted acoustic waves, as well as EM waves at the interface; the transmitted acoustic wave is accompanied by a quasi-static electric field in the sediment. By varying the NaCl concentration in the pore fluid between 0.0052 S/m and 0.12 S/m, we determined the conductivity dependence of (1) the electric potential localized within the support of the transmitted acoustic wave, and (2) the EM waves generated at the interface.

The various electric fields are measured by laboratory grade, sintered Ag/AgCl electrodes (A-M Systems) that are fixed in a vertical array both above and below the fluid-sediment interface at nine vertical positions. The apparatus consists of a PVC tube, half-filled with de-ionized (DI) water in which NaCl is dissolved, and half-filled with glass microspheres or medium-grain sand saturated by this electrolyte. The saturating fluid is drained from below and simultaneously replenished from above with a different NaCl solution after each measurement sequence, and the sediment is kept fully saturated throughout this process.

A 100 kHz (center frequency) submersible acoustic transducer at the top of the apparatus is controlled by a data acquisition PC and driven with a 50 kHz sine-wave burst for approximately 60 μs . While the amplitude of the transmitted wave is not a maximum

at this operating frequency, the seismoelectric response levels, which decrease with increasing frequency, are largest for the 50 kHz burst. Short-time bursts for the transducer input signals ensure that the electrode responses are not due to electrical cross-talk. Electrode data is amplified 60 dB, averaged 1000 times for each measurement, and band-pass filtered between 2 kHz and 500 kHz to remove unwanted noise.

The entire apparatus is set inside a copper-mesh Faraday cage, which acts as common ground for one port of the 60 dB pre-amplifier, as well as for the other laboratory instruments (the transducer, PC, power amplifier, etc.). The copper-mesh cage increases signal-to-noise levels more than ten-fold, and therefore plays an important role in the experiment. See the figure caption for further details. In a separate calibration measurement, we determined the pressure waveform of the incident acoustic wave at the position of a (virtual) fluid-sediment interface by fixing a hydrophone at the end of a one-meter portion of the PVC tube.

3.2 Discussion of a Typical Data Set

Figures 3(a) and 3(b) depict seismoelectric potentials measured for the 50 kHz sine-wave burst in loose glass microspheres saturated by a NaCl solution with a pore-fluid conductivity of 0.0052 S/m. A number of separate arrivals can be distinguished. Arrivals occur near 750 μ s in both the water and sediment, almost simultaneously at each of the electrodes along the vertical array. These signals correspond to EM waves in the fluid and sediment—they are generated at the fluid-sediment interface and propagate at the speed of light in each medium. Similar observations of EM waves in consolidated porous rock and sandstone are well documented [*Beamish, 1999*], and are similar in magnitude

to the EM waves observed in our glass and sand data. Figure 3(a) also shows that electrodes above the fluid-sediment interface measure a small voltage that is coincident with the first passage of the incident acoustic wave, perhaps caused by a pressure-wave disturbance of the double layers formed on each electrode. Saturated medium-grain sand exhibits the same qualitative features; Figures 4(a) and 4(b) depict the seismoelectric-response levels in sand using a pore-fluid conductivity of 0.0076 S/m.

The second arrivals in Figures 3(b) and 4(b) are seen to move out with increasing depth in the model sediments. Comparing arrival times for electrodes #7 and #9 leads to estimated wavespeeds of 1730 m/s and 1690 m/s (at 50 kHz) for the second arrival in glass microspheres and medium-grain sand, respectively. We also applied a matched filter technique with a broad-band chirp (in the 10 – 800 kHz band, using electrodes #3 and #8) to calculate group velocities of approximately 1770 m/s for both sand and glass microspheres. These values are typical of the wavespeeds of the Biot fast wave in unconsolidated sediments within this frequency range (see *Stoll* [1983], for example). Accordingly, we believe the second arrival is essentially a plane, Biot fast wave.

We are unable to discern any Biot slow waves or shear waves in the data (but slow-wave motion is essentially diffusive in unconsolidated media [*Johnson and Plona*, 1982]); separate arrivals from higher-order modes in the sediment tube are also difficult to detect. The seismoelectric potentials coincident with the fast-wave arrival are generally less than 1 mV and decrease monotonically with increasing NaCl concentration, for the range of conductivities tested. Figure 5 depicts this behavior, using electrode #8, for the 50 kHz sine-wave burst in glass microspheres over the full range of conductivities.

3.3 Bulk and Pore-Fluid Conductivity

The coupled EK-Biot theory described in Section 2 yields an expression of the bulk sediment conductivity,

$$\sigma_{bulk}(\omega) = \frac{\phi}{\alpha_\infty} \left[\sigma_f + \frac{2\Sigma(\omega)}{\Lambda} \right], \quad (6)$$

in terms of the pore-fluid conductivity σ_f , pore-throat dimension Λ (often a fixed fraction of the grain diameter), and surface conductance of the diffuse layer Σ . Coupled EK-Biot theory provides an explicit relationship between Σ and two forms of surface conduction (frequency-dependent electroosmosis and electromigration; see Eqn. (242) in *Pride [1994]*). Because the $\sigma_{bulk} - \sigma_f$ relation plays a critical role in determining seismoelectric behavior, each conduction mechanism must be accurately accounted for in order to compare numerical predictions to experimental data.

Another issue is chemical equilibration in the pore space. The conductivity of the solution used to saturate the sediments (which we denote by σ_w) increases rapidly until it plateaus at the value of the equilibrium *in situ* pore-fluid conductivity σ_f ; equilibration often occurs within a few hours and is only apparent for $\sigma_w \leq 0.01$ S/m. The *pH* of the pore-fluid showed a similar increase from *pH* 7 to *pH* 8.5 – 9 during this time. Append B details a treatment process that helped stabilize the grain surface chemistry of our samples. A separate study of the equilibration behavior provided a means of determining σ_f from known values of σ_w ; our results also showed that (1) chemical equilibration was substantially reduced for the treated samples, and (2) allowing for sufficient time

between runs (greater than four hours) would minimize the effect of this variability on our experimental data [Block, 2004].

Before each run, an HP 4192A impedance analyzer is used to determine the electrical impedance (at 1 kHz) of the fluid above the water-sediment interface (between electrodes #1 and #2) and within the sediment (between electrodes #7 and #8). The impedances are then converted to conductivities following a straightforward calibration procedure [Block, 2004]; the resulting data is summarized in Figure 6. The $\sigma_{bulk} - \sigma_f$ relation that affects seismoelectric response follows an almost linear trend for both medium-grain sand (“*”) and loose glass microspheres (“+”). However, there is a noticeable shift away from linearity for the weakest electrolytes. As expected, the $\sigma_{bulk} - \sigma_w$ relation (indicated by symbols with holes in their centers) is strongly nonlinear. Figure 6 also includes two glass data points that correspond to the same input fluid conductivity, σ_w : although DI water was used in both cases, one point corresponds to 16 hours of equilibration (diamond), while the other corresponds to an equilibration time of only 4 hours. Error ellipses represent two standard deviations from the mean.

Although *Pride’s* [1994] theory predicts a negligible contribution from the surface conductance Σ for the range of pore-fluid conductivities that we tested, other researchers found experimental evidence that σ_{bulk} is significantly affected by surface conduction in sandstones [Glover *et al.*, 1994; Nettelblad *et al.*, 1995] and clay-bearing sands [Wildenschild *et al.*, 2000] containing just 1 – 3 % clay. A small amount of clay and silt was present in our sand, even after numerous runs. For reasons that we explain in Section 5, we chose a fitted value of $\Sigma = 4.16 \times 10^{-8}$ S to match *both* the bulk conductivity data and seismoelectric data for our medium-grain sand (dashed curve in Figure 6). This value

of Σ is approximately one fifth the value that *Wildenschild et al.* [2000] found for their cleaned Ottawa sand samples. To compare and contrast these results with the unmodified form of EK-Biot theory, we used the explicit version of Σ derived by *Pride* [1994] to interpret our measurements using loose glass microspheres (solid curve).

Equation (6) also allows us to determine the formation factor, $F \equiv \alpha_{\infty} / \phi \approx 4$, from the inverse of the slope of the solid curve in the large-conductivity limit. This approximate value of F is within the expected range of 3.5 to 5 that is observed in sediments with similar grain sizes. Following *Williams et al.* [2002], who measured porosities of between 0.36 and 0.40 for medium grain sand, we assumed $\phi \approx 0.38$ for both media. Then the tortuosity is estimated to be: $\alpha_{\infty} \approx 1.52$, which is also within the expected range of 1.35 to 2.25 for unconsolidated ocean sediments.

4 Numerical Modeling

To predict the signal received at each electrode, we determine all of the electromagnetic disturbances that result from an acoustic plane wave scattering from an EK-Biot half-space. Assuming that the incident wave is plane and that the wall does not affect the incident and scattered waves is a reasonable approximation because the group velocities are very close to their plane-wave counterparts, and little dispersive behavior was seen in Figures 3 and 4. Accordingly, we expect that only the lowest-order mode is significant in our data and that it approximates a plane wave.

Another simplification results from the fact that the electrokinetic coupling in our experiment is predominantly one way: While the incident pressure wave generates pore-

fluid motion and hence a measurable electric field, the secondary pore-fluid motion that would result from this electric field is negligible. This statement within EK-Biot theory is equivalent to the approximation that

$$\left| \frac{\eta L^2(\omega)}{k(\omega)} \right| \ll |\sigma_{bulk}(\omega) - i\omega \varepsilon_{bulk}|, \quad (7)$$

which we assume here. Note that ε_{bulk} is given by (4), the role of $L(\omega)$, $k(\omega)$, and η are indicated by (5), and $\sigma_{bulk}(\omega)$ is defined in (6). We calculate the relative fluid motion vector $\bar{\mathbf{w}}$ independently of the EM fields by first solving the simpler problem of reflection from a Biot half-space. At the fluid-sediment interface, relative fluid motion in the EM boundary conditions acts as a source (a layer of dipoles) for an electromagnetic wave; this is the origin of the EM wave noted in our experimental results. The transmitted acoustic wave in the sediment also generates a quasi-static electric field within its support, as indicated previously.

4.1 Reflection from a Fluid-Sediment Interface

The Biot reflection problem is solved by *Stoll* [1981] and *Stern et al.* [1985]. This analysis results in vector and scalar potentials within the fluid and sediment (Eqns. (63) – (67) in *Stern et al.* [1985]), from which it is straightforward to calculate the relative fluid displacement at the interface, namely,

$$\bar{\mathbf{w}} = \bar{\mathbf{w}}(\theta_w) p_w|_{z=0}, \quad (8)$$

for a given time-harmonic component of the acoustic pressure p_w incident at angle θ_w (additional dependencies on angular frequency ω and the fluid and sediment properties are implicit). We set $p_w|_{z=0} = 1$ for the moment. The total relative fluid displacement is

$$\bar{\mathbf{w}} = \bar{\mathbf{w}}_s + \bar{\mathbf{w}}_{pf} + \bar{\mathbf{w}}_{ps}, \quad (9)$$

where $\bar{\mathbf{w}}_s$ is the shear-wave contribution, and $\bar{\mathbf{w}}_{pf}$ and $\bar{\mathbf{w}}_{ps}$ are contributions from the fast and slow compressional waves, respectively. These terms act as sources for the electromagnetic waves in what follows.

As shown in Figure 7, unit wavevectors for the plane waves (for propagation in the x - z plane) are defined as:

$$\begin{aligned} \hat{\mathbf{k}}_w &= \cos \theta_w \hat{\mathbf{x}} + \sin \theta_w \hat{\mathbf{z}} \\ \hat{\mathbf{k}}_{rw} &= \cos \theta_{rw} \hat{\mathbf{x}} - \sin \theta_{rw} \hat{\mathbf{z}} \\ \hat{\mathbf{k}}_{ew} &= \cos \theta_{ew} \hat{\mathbf{x}} - \sin \theta_{ew} \hat{\mathbf{z}}, \end{aligned} \quad (10)$$

for the incident, reflected, and EM waves in water, respectively. The EM wavenumber $k_w = \omega / c_w$, where c_w is the phase velocity in water. In the sediment,

$$\begin{aligned} \hat{\mathbf{k}}_{eb} &= \cos \theta_{eb} \hat{\mathbf{x}} + \sin \theta_{eb} \hat{\mathbf{z}} \\ \hat{\mathbf{k}}_l &= \cos \theta_l \hat{\mathbf{x}} + \sin \theta_l \hat{\mathbf{z}}, \end{aligned} \quad (11)$$

where $l = s, pf$, and ps for the shear, fast, and slow waves, respectively. Wavenumbers for the EM modes, k_{ew} and k_{eb} , are defined shortly, while k_s , k_{pf} , and k_{ps} can be found in Eqns. (87) and (92) in *Pride and Haartsen* [1996]. Note that phase matching is enforced at the interface, so that an $\exp(ik_l \cos \theta_l x)$ dependence is found for each of the EM and mechanical wavefields.

Maxwell's equations in water are solved by setting

$$\bar{\mathbf{H}}_{ew} = \bar{\mathbf{h}}_{ew} \exp\left(ik_{ew} \hat{\mathbf{k}}_{ew} \cdot \hat{\mathbf{x}}\right) \quad (12)$$

and

$$\bar{\mathbf{E}}_{ew} = \bar{\mathbf{e}}_{ew} \exp\left(ik_{ew} \hat{\mathbf{k}}_{ew} \cdot \hat{\mathbf{x}}\right), \quad (13)$$

where

$$k_{ew} = \sqrt{i\omega\mu_0(\sigma_w - i\omega\epsilon_0\kappa_w)} \quad (14)$$

is the EM wavenumber in water. In the sediment, (3) and (5) lead to

$$\nabla^2 \bar{\mathbf{H}}_b + k_{eb}^2 \bar{\mathbf{H}}_b = \frac{i\omega\eta L}{k} \nabla \times \bar{\mathbf{w}}, \quad (15)$$

where

$$k_{eb} = \sqrt{i\omega\mu_0(\sigma_{bulk} - i\omega\epsilon_{bulk})} \quad (16)$$

is the so-called bare EM wavenumber in sediment. Because the EM fields do not generate mechanical motion (using the approximation in (7)), the EM wavenumber is determined by the sediment's electrical properties alone (the exact value is found by solving an eigenvalue problem derived from the fully coupled EK-Biot equations in *Pride and Haartsen* [1996]).

The magnetic field in the sediment is split into two parts, $\bar{\mathbf{H}}_b = \bar{\mathbf{H}}_{eb} + \bar{\mathbf{H}}_{mb}$. The first term is the transverse EM-wave,

$$\bar{\mathbf{H}}_{eb} = \bar{\mathbf{h}}_{eb} \exp\left(ik_{eb} \hat{\mathbf{k}}_{eb} \cdot \hat{\mathbf{x}}\right). \quad (17)$$

The second term is a mechanically induced part, $\bar{\mathbf{H}}_{mb}$, which is the particular solution to (15), namely,

$$\bar{\mathbf{H}}_{mb} = \frac{k_s}{(k_s^2 - k_{eb}^2)} \frac{\omega\eta L}{k} \hat{\mathbf{k}}_s \times \bar{\mathbf{w}}_s. \quad (18)$$

It is generated only by shear-wave motion, $\bar{\mathbf{w}}_s$.

The electric field solution in the sediment can also be separated into two parts,

$\bar{\mathbf{E}}_b = \bar{\mathbf{E}}_{eb} + \bar{\mathbf{E}}_{mb}$, where

$$\bar{\mathbf{E}}_{eb} = \bar{\mathbf{e}}_{eb} \exp\left(ik_{eb}\hat{\mathbf{k}}_{eb} \cdot \hat{\mathbf{x}}\right) \quad (19)$$

travels at the (bare) EM wavespeed in the sediment. It is then straightforward to determine that

$$\bar{\mathbf{E}}_{mb} = -\frac{\omega\mu_0}{k_{eb}^2} \frac{\omega\eta L}{k} \left[\bar{\mathbf{w}}_{pf} + \bar{\mathbf{w}}_{ps} - \frac{k_{eb}^2}{(k_s^2 - k_{eb}^2)} \bar{\mathbf{w}}_s \right], \quad (20)$$

using (3), (5), and (18). While $\bar{\mathbf{E}}_{mb}$ has components along each of the polarizations of the transmitted waves, the shear-wave contribution is negligible since $|k_s|^2 \ll |k_{eb}|^2$.

The mechanically induced electric and magnetic fields act as source terms in the EM boundary conditions at the water-sediment interface; thus,

$$\begin{aligned} \hat{\mathbf{z}} \times (\bar{\mathbf{E}}_{eb} - \bar{\mathbf{E}}_{ew}) \Big|_{z=0} &= -\hat{\mathbf{z}} \times \bar{\mathbf{E}}_{mb} \Big|_{z=0} \\ \hat{\mathbf{z}} \times (\bar{\mathbf{H}}_{eb} - \bar{\mathbf{H}}_{ew}) \Big|_{z=0} &= -\hat{\mathbf{z}} \times \bar{\mathbf{H}}_{mb} \Big|_{z=0}. \end{aligned} \quad (21)$$

We assume that the interface is uncharged prior to any disturbance, so that there are no additional charge or current sources in (21). Following *Haartsen and Pride* [1997], we treat only the case where the particle displacement is in the x - z plane: the PSVTM (pressure, shear-vertical, transverse magnetic) case. The electric fields $\bar{\mathbf{e}}_{ew}$ and $\bar{\mathbf{e}}_{eb}$ are determined by enforcing (21). A complete list of all the electric fields, both those carried along by the acoustic waves and those excited at the interface, are given in Eqns. (4.46) – (4.53) in *Block* [2004].

To determine the seismoelectric potentials along the electrode array, we set

$$\bar{\mathbf{E}}_{mb}^l = -\nabla V_{mb}^l = -i\mathbf{k}_l V_{mb}^l, \text{ with } l = pf \text{ and } ps, \text{ where}$$

$$V_{mb}^{pf} = -w_{pf} \left(\frac{\omega^2 \mu_0 \eta L}{k} \frac{i}{k_{pf} k_{eb}^2} \right) \exp(i k_{pf} \hat{\mathbf{k}}_{pf} \cdot \hat{\mathbf{x}}) \quad (22)$$

is the potential (or voltage) generated by a fast wave propagating in the sediment.

Similarly,

$$V_{mb}^{ps} = -w_{ps} \left(\frac{\omega^2 \mu_0 \eta L}{k} \frac{i}{k_{ps} k_{eb}^2} \right) \exp(i k_{ps} \hat{\mathbf{k}}_{ps} \cdot \hat{\mathbf{x}}) \quad (23)$$

is the potential (or voltage) generated by a slow wave propagating in the sediment. We plot V_{mb}^{ps} in the subsequent figures to compare it with the fast-wave potential, although we were unable to identify slow waves in our experimental data.

Transverse EM waves measured in water and sediment are also measured by the Ag/AgCl electrodes. We set $\bar{\mathbf{E}}_{eb}^l \cdot \hat{\mathbf{x}} = -i k_l V_{eb}^l$, with $l = pf$ and ps , where

$$\begin{aligned} V_{eb}^{pf} &= -w_{pf} \left(\frac{\omega^2 \mu_0 \eta L}{k} \frac{i k_{ew}}{k_{eb}^3} \right) \frac{\cos \theta_{pf} \exp(i k_{eb} \hat{\mathbf{k}}_{eb} \cdot \hat{\mathbf{x}})}{(k_{ew} \sin \theta_{eb} + k_{eb} \sin \theta_{ew})} \\ V_{ew}^{pf} &= -w_{pf} \left(\frac{\omega^2 \mu_0 \eta L}{k} \frac{i}{k_{ew} k_{eb}} \right) \frac{\cos \theta_{pf} \exp(i k_{ew} \hat{\mathbf{k}}_{ew} \cdot \hat{\mathbf{x}})}{(k_{ew} \sin \theta_{eb} + k_{eb} \sin \theta_{ew})}. \end{aligned} \quad (24)$$

Note that the potentials in (22), (23), and (24) are found directly in terms of the fast- and slow-wave components of the relative fluid displacements, w_{pf} and w_{ps} , respectively, which depend implicitly on the incident angle θ_w , angular frequency ω , and material properties of the fluid and bulk sediment.

4.2 Numerical Predictions

The predicted potentials, evaluated at $z = 0$, are plotted for various situations in the following figures. We have assumed the conductivities of the pore fluid and water above sediment to be equal for simplicity. The potentials have been scaled by the input pressure magnitude (at the interface), so that the y axes have units of nanoVolts per Pascal. Unless otherwise stated, the material properties are those found to best fit the experimental data shown in the next section and are those summarized in Appendix A.

Figures 8(a) and 8(b) depict how the magnitudes of the potentials vary with pore-fluid conductivity in medium-grain sand (using a constant surface conductance Σ) and loose glass microspheres (using the Σ derived by *Pride* [1994]), respectively. Both figures assume a fixed frequency $f = 50$ kHz and incident angle $\theta_w = \pi/2$. A peak is predicted for EM-wave potentials in sand when the contributions from surface and pore conduction balance, i.e., when $\sigma_f \approx 2.6 \times 10^{-3}$ S/m in (6). While the seismoelectric potentials are predicted to decay as $1/\sigma_f$ for large conductivities in both media, using the fitted surface conductance Σ lessens the seismoelectric response for weak electrolytes.

Figures 8(c) and 8(d) depict the behavior in medium-grain sand; the frequency and angle dependence of the potentials are qualitatively similar in both media. Figure 8(c) predicts that the fast-wave potential decays as $1/\sqrt{f}$ above the transition frequency defined in (A.6), but remains essentially constant for frequencies below this value. Because the EM-wave potentials peak near this frequency, broad-band measurements of EM phenomena might be used to determine pore-scale features, which are intimately connected with the transition frequency.

Figure 8(d) depicts the magnitudes of the potentials versus angle of incidence, where a strong increase is seen at the fast-wave critical angle (about 30°) for V_{mb}^{pf} , V_{eb}^{pf} , and V_{ew}^{pf} . One aspect of the plane-wave problem is that the EM-wave potentials exhibit a rapid decay to zero near normal incidence (within one degree for these sediments). This phenomenon is caused by the uniform dipole layer at the interface, but ceases to be an issue when there is a deviation from planarity (e.g., due to a slight angle in the sediment surface) or when the dipole layer exists only over a finite region (as in our apparatus).

5 Comparing Theory to Data

We use the peak magnitude of the second arrivals (as in Figures 3(b) and 4(b)) to compare our laboratory data to numerical predictions. To simulate fast-wave voltages at the position of electrode #8 in the sediment, we define

$$V_{predict} = V_{mb}^{pf} \left(\theta_w = \frac{\pi}{2}, z = 0.353 \text{ m} \right) p_w|_{z=0}, \quad (25)$$

using the Fourier transform of the measured 50 kHz signal, p_w . Note that w_{pf} is calculated per unit applied pressure: for a known p_w and sediment type, we use the Biot reflection problem to generate w_{pf} at normal incidence. A time series for the predicted voltage is then computed using (22) and (25) for the range of pore-fluid conductivities tested in the laboratory.

One of the main difficulties of comparing EK-Biot predictions to data is the number of parameters involved. The only parameters that we varied to fit the data, by estimation

and trial and error, were the DC permeability k_0 and the ζ potential. The Kozeny-Carman relation [Johnson *et al.*, 1987],

$$\Lambda = \sqrt{\frac{8k_0\alpha_\infty}{\phi}}, \quad (26)$$

was used to relate k_0 to the pore-throat dimension Λ , tortuosity α_∞ , and volume fraction ϕ . This is an experimentally determined relationship that is approximately valid for these sediments. Sand and glass microspheres were assumed to have the same values for the other EK-Biot parameters. Also, while the ζ potential is known to depend on pore-fluid conductivity and pH [Ishido and Mizutani, 1981], best-fit values for both sand and glass microspheres were $\zeta \approx -40$ mV, which is near the lower range for silica over this range of conductivities (and at pH 9). Best-fit values for the DC permeabilities were $k_0 \approx 8 \times 10^{-12} \text{ m}^2$ for medium-grain sand and $k_0 \approx 11 \times 10^{-12} \text{ m}^2$ for loose glass microspheres. Equation (26) predicts effective pore radii for sand and glass to be approximately $\Lambda \approx 16 \text{ } \mu\text{m}$ and $\Lambda \approx 19 \text{ } \mu\text{m}$, respectively.

Figure 9 shows the results of comparing the peaks of the fast-wave potential at electrode #8 for both data and theory. Error ellipses represent two standard deviations from the mean. The fit for glass microspheres (solid curve) is based on the unmodified form of EK-Biot theory, while the predictions for medium-grain sand (dashed curve) rely on a fitted value of the surface conductance Σ to simultaneously match both the fast-wave voltage and bulk conductivity data. Individual data points are accurately predicted and there is a clear similarity between theoretical and experimental trends for both curves. The unmodified form of EK-Biot theory predicts that the magnitude of the seismoelectric potential increases as the conductivity is lowered, and this trend is

exhibited by the glass data. However, seismoelectric potentials in medium-grain sand appear to grow less rapidly at lower conductivities. Combining the fitted surface conductance Σ with EK-Biot theory allowed us to predict this feature.

Because EK-Biot theory is a broad-band model—in contrast to the other EK models discussed in Section 2.2, which hold only in the low-frequency limit—we are able to compare our high-frequency results to the data of *Ahmed* [1964], who measured EK voltages generated by constant flow rates in sand and loose glass microspheres, and *Pengra and Wong* [1999], who studied low-frequency EK behavior in consolidated porous media. The results shown here fall within the ranges of both datasets (see *Block* [2004] for details), which provides another argument for the reliability of EK-Biot theory ((5), in particular) and the plane-wave model described in Section 4.

6 Summary and Conclusions

Medium-grain sand and loose glass microspheres were studied using pore-fluid conductivities that ranged between 0.0052 S/m and 0.12 S/m. Electrodes buried in the sediment measure two types of seismoelectric phenomena: (1) arrivals from an EM wave generated at the interface, which is recorded at all electrodes simultaneously, and (2) electric potentials carried along with transmitted acoustic waves in the sediment. Electrodes above the water-sediment interface measure the EM-wave arrival in water, as well as a small disturbance of the electrode double layers caused by the incident acoustic wave. Fast-wave potentials in the sediments are often greater than 500 μV , while the EM-wave potentials are usually 100 μV in magnitude. These values correspond to efficiencies greater than 150 nV/Pa and 30 nV/Pa, at 50 kHz, respectively.

EK-Biot theory is able to predict the trends and magnitudes of the laboratory data with good accuracy for a large range of pore-fluid conductivities. But we emphasize that a robust model of $\sigma_{bulk}(\sigma_f)$ is critical for field applications that utilize electrokinetic and conductivity data from clay-bearing sands and sandstones. The results from seismic-electric (and electroseismic) imaging of oil and gas reservoirs may also be affected when EM-wave phenomena are used to determine the properties of rocks saturated by fresh water and/or hydrocarbons.

The implications of our results in the field of ocean seabed acoustics are twofold. First, a clear distinction can be made between the kinematics of poroelasticity and that of other theories. The viscoelastic fluid and solid models that are commonly used rely on a single, macroscopic displacement field because the dynamics of the separate phases are lost (or ignored) while upscaling. In contrast, poroelasticity allows the fluid and solid frame to undergo relative motion and preserves this two-phase behavior on the macroscale. The resulting dissipation mechanism depends on the *average* relative fluid displacement ($\bar{\mathbf{w}}$), which plays a critical role in both acoustic and seismoelectric behavior—theories that do not retain this mechanism are incapable of predicting the EK phenomena described here. We can turn this argument around: because sediments are well-modeled by EK-Biot theory, they should also exhibit Biot properties in situations where the pore fluid is not an electrolyte (i.e., with $L(\omega) \equiv 0$).

Second, experimentally derived (*ad hoc*) models of the seabed offer no details on how wave propagation depends on sediment microstructure. Rigorous averaging is not only more powerful—by providing a direct connection between effective-medium and pore-scale properties—but it is essential to predicting key experimental behaviors, such as

EM-wave generation at a fluid-sediment interface and the broad-band frequency dependence of seismoelectric phenomena, that are a robust feature in our data.

Acknowledgements

The work of G. Block was supported by the Office of Naval Research, Department of Ocean, Atmosphere and Space Sciences, under contract N00014-02-1-0335, and under the auspices of the U.S. Department of Energy by UC, LLNL under contract W-7405-ENG-48, supported specifically by the Geosciences Research Program of the DOE Office of Basic Energy Sciences, Division of Chemical Sciences, Geosciences and Biosciences. The authors also wish to thank the Applied Research Laboratory at the University of Texas at Austin, N.P. Chotiros, and J.G. Berryman.

Appendix A: Material Properties

The material properties for our sediment samples are given in Table 1. The DC permeability k_0 , pore-throat dimension Λ , and ζ potential are determined by parameter fits and the Kozeny-Carman relation (26), as described in Section 5. Medium-grain sand (mesh #4 sand-blasting sand) and glass microspheres (lead-free, borosilicate glass from Glen Mills, Inc., NJ) have grain diameters of approximately 250 μm and 350 μm , respectively.

The constitutive relations for two-phase, isotropic poroelastic media (see *Pride et al.* [1992]) are as follows:

$$\begin{aligned}\boldsymbol{\tau}_{bulk} &= (K_G \nabla \cdot \bar{\mathbf{u}}_s + C \nabla \cdot \bar{\mathbf{w}}) \mathbf{I} + G_{fr} \left(\nabla \bar{\mathbf{u}}_s + \nabla \bar{\mathbf{u}}_s^T - \frac{2}{3} \nabla \cdot \bar{\mathbf{u}}_s \mathbf{I} \right) \\ -p &= C \nabla \cdot \bar{\mathbf{u}}_s + M \nabla \cdot \bar{\mathbf{w}},\end{aligned}\tag{A.1}$$

where

$$\begin{aligned}K_G &= \frac{K_{fr} + \phi K_f + (1 + \phi) K_s \Delta}{1 + \Delta} \\ C &= \frac{K_f + K_s \Delta}{1 + \Delta} \\ M &= \frac{1}{\phi} \frac{K_f}{1 + \Delta},\end{aligned}\tag{A.2}$$

and the parameter Δ is

$$\Delta = \frac{K_f}{\phi K_s} \left[(1 - \phi) K_s - K_{fr} \right].\tag{A.3}$$

The bulk and shear frame moduli of the sediment, K_{fr} and G_{fr} , respectively, are often assumed complex to model for inelastic behavior that is not accounted for by Biot theory; we assumed that both media had the same frame properties, and chose their values in accordance with the accepted range discussed in the ocean acoustics literature.

The dynamic Darcy permeability,

$$\frac{k(\omega)}{k_0} = \left[\left(1 - i \frac{\omega}{\omega_t} \frac{4}{m} \right)^{1/2} - i \frac{\omega}{\omega_t} \right],\tag{A.4}$$

is derived in *Pride* [1994]. Here, k_0 is the DC permeability,

$$m = \frac{\phi}{\alpha_\infty \eta} \Lambda^2,\tag{A.5}$$

and

$$\omega_t = \frac{\phi}{\alpha_\infty k_0} \frac{\eta}{\rho_f}\tag{A.6}$$

is the Biot transition frequency discussed in Sections 2 and 5.

The EK coupling coefficient [Pride, 1994] using the Debye approximation takes the form:

$$\frac{L(\omega)}{L_0} = \left[1 - i \frac{\omega}{\omega_t} \frac{m}{4} \left(1 - 2 \frac{d}{\Lambda} \right)^2 \left(1 - i^{3/2} d \sqrt{\frac{\omega \rho_f}{\eta}} \right) \right], \quad (\text{A.7})$$

where

$$L_0 = - \frac{\phi}{\alpha_\infty} \frac{\varepsilon_0 \kappa_f \zeta}{\eta} \left(1 - 2 \frac{d}{\Lambda} \right). \quad (\text{A.8})$$

The Debye length in a NaCl solution,

$$d = \sqrt{\frac{\varepsilon_0 \kappa_f k_B T}{2 \sigma_f}} (b_{Na} + b_{Cl}), \quad (\text{A.9})$$

characterizes the thickness of the electric double layer, and is generally less than 10 nm;

it depends on Boltzmann's constant k_B (1.38×10^{-23} J/K), the ambient temperature

T (298 K), the pore-fluid conductivity σ_f , and the ionic mobilities of Na^+ and Cl^- ,

b_{Na} and b_{Cl} , respectively.

Table 1: Water and sediment (sand & glass) properties

K_f (GPa)	2.4		α_∞	1.52
K_s (GPa)	32		ϕ	0.38
K_{fr} (MPa)	$44(1+0.06i)$		κ_f	80
G_{fr} (MPa)	$29(1+0.05i)$		κ_s	3
ρ_s (kg/m ³)	2650		ζ (mV)	-40
ρ_f (kg/m ³)	1023		b_{Na} (s/kg)	2.9×10^{11}
η (kg/ms)	10^{-3}		b_{Cl} (s/kg)	4.4×10^{11}
k_0 (μm^2)	8 & 11		μ_0 (H/m)	10^{-3}
Λ (μm)	16 & 19		ε_0 (F/m)	8.85×10^{-12}

Appendix B: Sample Characterization

Both the surface charge density and ζ potential of naturally occurring silica are often reduced by adsorption of organic material and/or the recombination of partially-bound oxygen to neighboring silicon atoms. We attempted to stabilize the surface-chemical properties and maximize the surface-charge density of our samples following *Hau et al.* [2003]. The samples were rinsed with de-ionized water after each step. A strong sulfuric acid was used to remove organic impurities (15% by vol. at 100 °C for 30 min.). Next, the sample was rinsed with sodium hydroxide (10% by vol. at 100 °C for 30 min.) so that each hydroxide ion hydrolyzed SiO_2 to form silanol and silanol salt groups. Hydrochloric acid (10% by vol. at 100 °C for 30 min.) was then applied to displace the Na^+ ions, yielding mainly silanol groups. After interaction with water, $\text{pH } 7 - 8$, the silanol groups were deprotonated to produce a maximal density of unbound oxygen on the surface (and hence a maximal ζ potential).

The entire procedure was expected to produce a negatively charged surface with ζ potentials of approximately -65 mV at neutral pH . While chemical treatment stabilizes the surface-chemical properties of the samples and helped to minimize the effects of equilibration discussed in Section 3.3, both untreated and treated samples exhibited the same fast-wave potential levels (and had best-fit values of $\zeta \approx -40$ mV). The seismoelectric datasets discussed in this paper are based entirely on the treated samples.

References

- Ahmed, M. U. (1964), A laboratory study of streaming potentials, *Geophys. Prosp.*, *12*, 49-64.
- Auriault, J. L. and T. Strzelecki (1981), On the electro-osmotic flow in a saturated porous medium, *Int. J. Eng. Sc.*, *19*, 915-928.
- Beamish, D. (1999), Characteristics of near-surface electrokinetic coupling, *Geophys. J. Int.*, *137*, 231-242.
- Biot, M. A. (1956a), Theory of propagation of elastic waves in a fluid saturated porous solid I. Low frequency range, *J. Acoust. Soc. Am.*, *28*, 168-178.
- Biot, M. A. (1956b), Theory of propagation of elastic waves in a fluid saturated porous solid II. Higher frequency range, *J. Acoust. Soc. Am.*, *28*, 179-191.
- Biot, M. A. (1962), Mechanics of deformation and acoustic propagation in porous media, *J. Appl. Phys.*, *33*, 1482-1498.
- Block, G. (2004), Coupled acoustic and electromagnetic disturbances in a granular material saturated by a fluid electrolyte, University of Illinois at Urbana-Champaign, Champaign, Illinois.
- Buckingham, M. J. (1997), Theory of acoustic attenuation, dispersion, and pulse propagation in unconsolidated granular materials including marine sediments, *J. Acoust. Soc. Am.*, *102*, 2579-2596.
- Buckingham, M. J. (1998), Theory of compressional and shear waves in fluid-like marine sediments, *J. Acoust. Soc. Am.*, *103*, 288-299.
- Buckingham, M. J. (2005), Compressional and shear wave properties of marine sediments: Comparisons between theory and data, *J. Acoust. Soc. Am.*, *117*, 137-152.
- Chandler, R. N. (1981), Transient streaming potential measurements on fluid-saturated porous structures: an experimental verification of Biot's slow wave in the quasi-static limit, *J. Acoust. Soc. Am.*, *70*, 116-121.
- Chotiros, N. P. (1995), Biot model of sound propagation in water-saturated sand, *J. Acoust. Soc. Am.*, *97*, 199-214.
- Chotiros, N. P. and M. J. Isakson (2004), A broadband model of sandy ocean sediments: Biot-Stoll with contact squirt flow and shear drag, *J. Acoust. Soc. Am.*, *116*, 2011-2022.
- Debye, P. and E. Huckel (1923), On the theory of electrolytes. I. Freezing point depression and related phenomena, *Physikalische Zeitschrift*, *24*, 185-206.
- Dvorkin, J. and A. Nur (1993), Dynamic poroelasticity: A unified model with the squirt and the Biot mechanisms, *Geophysics*, *58*, 524-533.
- Fitterman, D. V. (1978), Electrokinetic and magnetic anomalies associated with dilatant regions in a layered Earth, *J. Geophys. Res.*, *83*, 5923-5928.
- Frenkel, J. (1944), On the theory of seismic and seismoelectric phenomena in moist soil, *J. Physics (Soviet)*, *8*, 230-241.
- Glover, P. W. J., P. G. Meredith, P. R. Sammonds, and S. A. F. Murrell (1994), Ionic surface electrical conductivity in sandstone, *J. Geophys. Res.*, *99*, 21635-21650.
- Gouy, G. (1910), About the electric charge on the surface of an electrolyte, *J. Phys. A*, *9*, 457-468.

- Haartsen, M. W. and S. R. Pride (1997), Electroseismic waves from point sources in layered media, *J. Geophys. Res.*, *102*, 24745-24769.
- Haartsen, M. W. and M. N. Toksöz (1996), Dynamic streaming currents from seismic point sources in homogeneous poro-elastic media, *Geophys. J. Int.*, *132*, 256-274.
- Hamilton, E. L. (1972), Compressional-wave attenuation in marine sediments, *Geophysics*, *37*, 620-646.
- Hamilton, E. L., (1974), Prediction of deep-sea sediment properties: state-of-the-art, in *Deep-sea sediments: physical and mechanical properties*, Inderbitzen, A. K., pp. 1-44, Plenum Press, New York.
- Hau, W. J. W., D. W. Trau, N. J. Sucher, M. Wong, and Y. Zohar (2003), Surface-chemistry technology for microfluidics, *J. Micromech. Microeng.*, *13*, 272-278.
- Hiemenz, P. and R. Rajagopalan (1997), *Principles of colloid and surface chemistry*, Marcel Dekker, Inc. New York.
- Ishido, T. and H. Mizutani (1981), Experimental and theoretical basis of electrokinetic phenomena in rock-water systems and its applications to geophysics, *J. Geophys. Res.*, *86*, 1763-1775.
- Johnson, D. L., J. Koplik, and R. Dashen (1987), Theory of dynamic permeability and tortuosity in fluid-saturated porous media, *J. Fluid Mech.*, *176*, 379-402.
- Johnson, D. L. and T. J. Plona (1982), Acoustic slow waves and the consolidation transition, *J. Acoust. Soc. Am.*, *72*, 556-565.
- Mikhailov, O. V., M. W. Haartsen, and M. N. Toksöz (1997), Electroseismic investigation of the shallow subsurface: field measurements and numerical modeling, *Geophysics*, *62*, 97-105.
- Murphy, W. F., K. W. Winkler, and R. L. Kleinberg (1986), Acoustic relaxation in sedimentary rocks: dependence on grain contacts and fluid saturation, *Geophysics*, *51*, 757-766.
- Neev, J. and F. R. Yeats (1989), Electrokinetic effects in fluid-saturated poroelastic media, *Phys. Rev. B*, *40*, 9135-9141.
- Nettelblad, B., B. Ahlen, G. A. Niklasson, and R. M. Holt (1995), Approximate determination of surface conductivity in porous media, *J. Phys. D: Appl. Phys.*, *28*, 2037-2045.
- O'Brien, R. W. (1988), Electro-acoustic effects in a dilute suspension of spherical particles, *J. Fluid Mech.*, *190*, 71-86.
- Pengra, D., S. X. Li, and P. Wong (1999), Determination of rock properties by low-frequency AC electrokinetics, *J. Geophys. Res.*, *104*, 485-508.
- Pengra, D. and P. Wong, (1995), Pore size, permeability and electrokinetic phenomena, in *Access in nanoporous materials*, Pinnavaia, T. J. and Tho, M. F., pp. 295-317, Plenum Press, New York.
- Pride, S. R. (1994), Governing equations for the coupled electromagnetics and acoustics of porous media, *Phys. Rev. B*, *50*, 15678-15696.
- Pride, S. R., A. F. Gangi, and F. D. Morgan (1992), Deriving the equations of motion for porous isotropic media, *J. Acoust. Soc. Am.*, *92*, 3278-3290.
- Pride, S. R. and M. W. Haartsen (1996), Electroseismic wave properties, *J. Acoust. Soc. Am.*, *100*, 1301-

1315.

- Rice, C. L. and R. Whitehead (1965), Electrokinetic flow in a narrow cylindrical capillary, *J. Phys. Chem.*, *69*, 4017-4024.
- Slattery, J. C. (1967), Flow of viscoelastic fluids through porous media, *Am. Ch. Eng. Journal*, *13*, 1066-1071.
- Stern, M., A. Bedford, and H. R. Millwater (1985), Wave reflection from a sediment layer with depth-dependent properties, *J. Acoust. Soc. Am.*, *77*, 1781-1788.
- Stern, O. (1924), The theory of the electrolytic double layer, *Zeitschrift für Elektrochemie*, *30*, 508-516.
- Stoll, R. D. (1981), Reflection of acoustic waves at a water-sediment interface, *J. Acoust. Soc. Am.*, *70*, 149-157.
- Stoll, R. D. (1983), *Sediment Acoustics*, Lecture Notes in Earth Science, Springer Verlag, Berlin.
- Stoll, R. D. (2002), Velocity dispersion in water-saturated granular sediment, *J. Acoust. Soc. Am.*, *111*, 785-793.
- Thompson, A. H. and G. A. Gist (1991), Electroseismic prospecting, *SEG Expanded Abstract, EM 2.1*, 425-427.
- Tutuncu, A. N. and M. M. Sharma (1992), The influence of fluids on grain contact stiffness and frame moduli in sedimentary rocks, *Geophysics*, *57*, 1571-1582.
- Wildenschild, D., J. J. Roberts, and E. D. Carlberg (2000), On the relationship between microstructure and electrical and hydraulic properties of sand-clay mixtures, *Geophys. Res. Lett.*, *27*, 3085-3088.
- Williams, K. L. (2001), An effective density fluid model for acoustic propagation in sediments derived from Biot theory, *J. Acoust. Soc. Am.*, *110*, 2276-2281.
- Williams, K. L., D. R. Jackson, E. I. Thorsos, D. Tang, and S. G. Schock (2002), Comparison of sound speed and attenuation measured in a sandy sediment to predictions based on the Biot theory of porous media, *IEEE J. Ocean Eng.*, *27*, 413-428.
- Zhu, Z., M. W. Haartsen, and M. N. Toksöz (1999), Experimental studies of electrokinetic conversions in fluid-saturated borehole models, *Geophysics*, *64*, 1349-1356.

Figure Captions

Figure 1: Electric double layer near a grain surface. Electrokinetics and fluid motion are coupled by the diffuse layer, which is free to move with the pore fluid.

Figure 2: Seismoelectric apparatus. The apparatus is based on a cylindrical tube geometry that is 7.62 cm in diameter. Ag/AgCl electrodes are buried in a vertical array within the sediment and above the water-sediment interface. A copper-mesh Faraday cage was used to isolate the apparatus from electrical interference and provide a universal ground. The transducer face diameter is 2.54 cm. Electrode and interface positions are accurate to 0.5 cm and 1 cm (between sample changes), respectively.

Figure 3: Loose glass microspheres at 0.0052 S/m. Electrodes measure (a) a simultaneous EM wave arrival in the fluid, as well as an additional response caused by an acoustic-wave disturbance of the electrolyte around each electrode, and (b) two arrivals in sediment: an EM wave arriving simultaneously at all electrodes, and a potential coupled to the transmitted wave, that moves out in time with deeper depths.

Figure 4: Medium-grain sand at 0.0076 S/m. Seismoelectric responses depicted in (a) and (b) are qualitatively similar to those observed in Figure 3, although smaller in amplitude.

Figure 5: Electrokinetic voltages for a range of conductivities for electrode #8 (buried in loose glass microspheres). Time series for conductivities between 0.0052 S/m and 0.12 S/m have been superposed.

Figure 6: Bulk versus pore-fluid conductivity for medium-grain sand ("*") and loose glass microspheres ("+"). The $\sigma_{bulk} - \sigma_f$ relation that affects seismoelectric response follows an almost linear trend for both sample types. As expected, the $\sigma_{bulk} - \sigma_w$ relation (indicated by symbols with holes in their centers) is strongly nonlinear. Predictions using a fitted surface conductance for sand (dashed curved) are compared to the unmodified form of EK-Biot theory for glass microspheres (solid curve). The diamond corresponds to glass microspheres saturated with DI water after 16 hours of equilibration. Error ellipses represent two standard deviations from the mean.

Figure 7: Reflection from an EK-Biot half-space produced by an incident pressure wave in water with wavevector $\hat{\mathbf{k}}_w$ and angle θ_w (relative to the horizontal axis). Two waves in the water are generated: a reflected acoustic wave ($\hat{\mathbf{k}}_{rw}$) and an EM wave ($\hat{\mathbf{k}}_{ew}$), and four waves in the sediment: slow ($\hat{\mathbf{k}}_{ps}$), shear ($\hat{\mathbf{k}}_s$), fast ($\hat{\mathbf{k}}_{pf}$), and an EM wave ($\hat{\mathbf{k}}_{eb}$).

Figure 8: Numerical predictions of seismoelectric potentials near a water-sediment interface versus pore-fluid conductivity in (a) medium-grain sand, and (b) loose glass microspheres, with frequency $f = 50$ kHz and $\theta_w = \pi/2$. (c) Potentials versus frequency in medium-grain sand, with $\theta_w = \pi/2$ and $\sigma_f = 0.01$ S/m. (d) Potentials versus angle of incidence in medium-grain sand, with $f = 50$ kHz and $\sigma_f = 0.01$ S/m.

Figure 9: Peaks of the fast-wave potentials (measured at electrode #8) versus the bulk conductivity. Data points for medium-grain sand ("*") and loose glass microspheres ("+") are compared to predictions for sand (dashed curved), based on a fitted surface conductance, and to glass (solid curve), using the unmodified form of EK-Biot theory. The diamond corresponds to glass microspheres saturated with DI water after 16 hours of equilibration. Error ellipses represent two standard deviations from the mean.

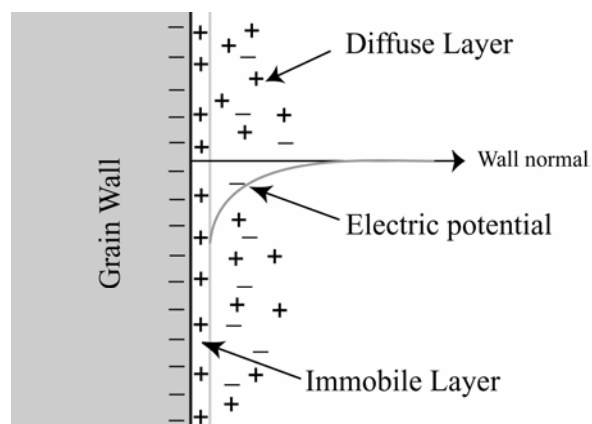


Figure 1

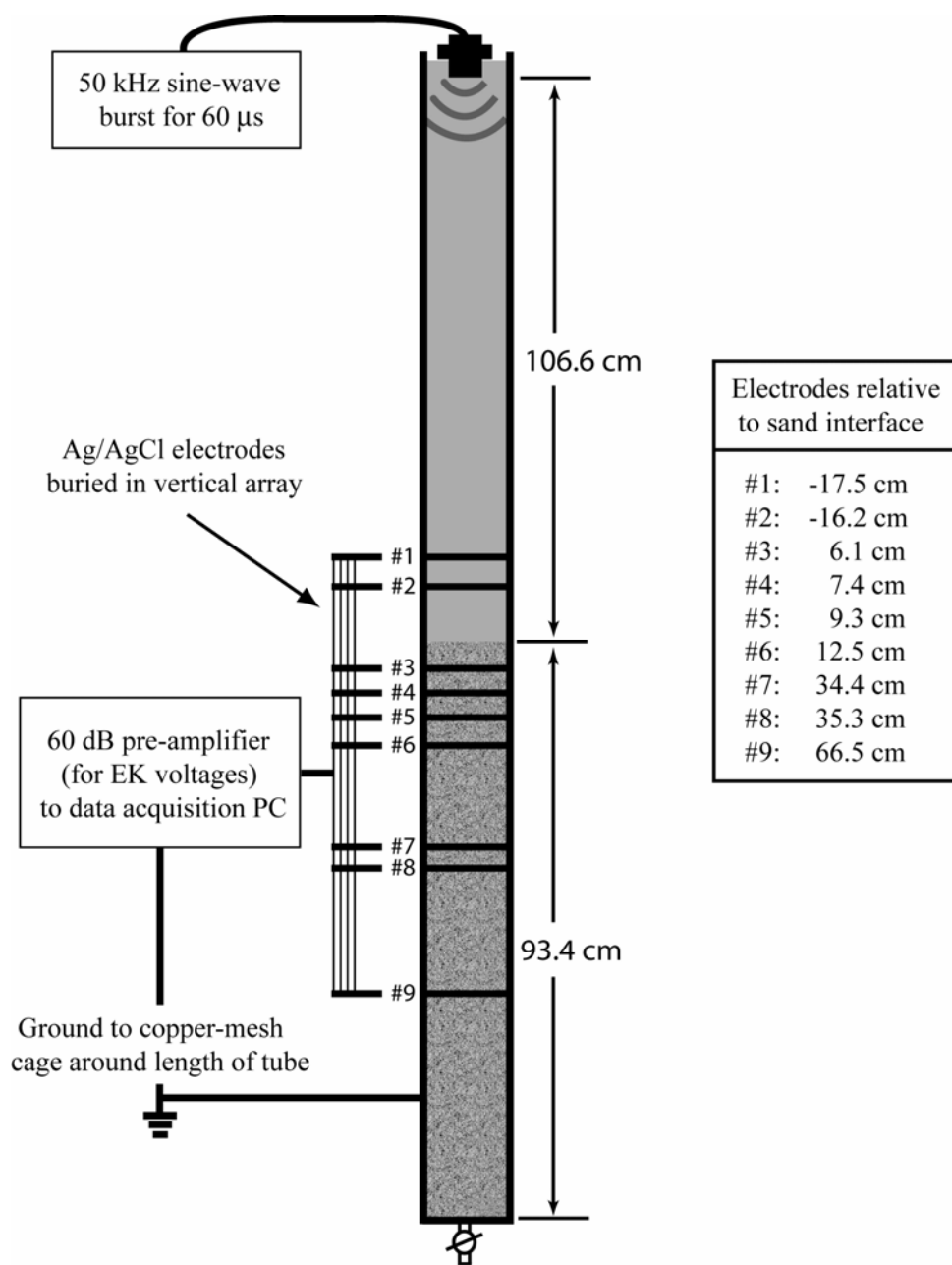


Figure 2

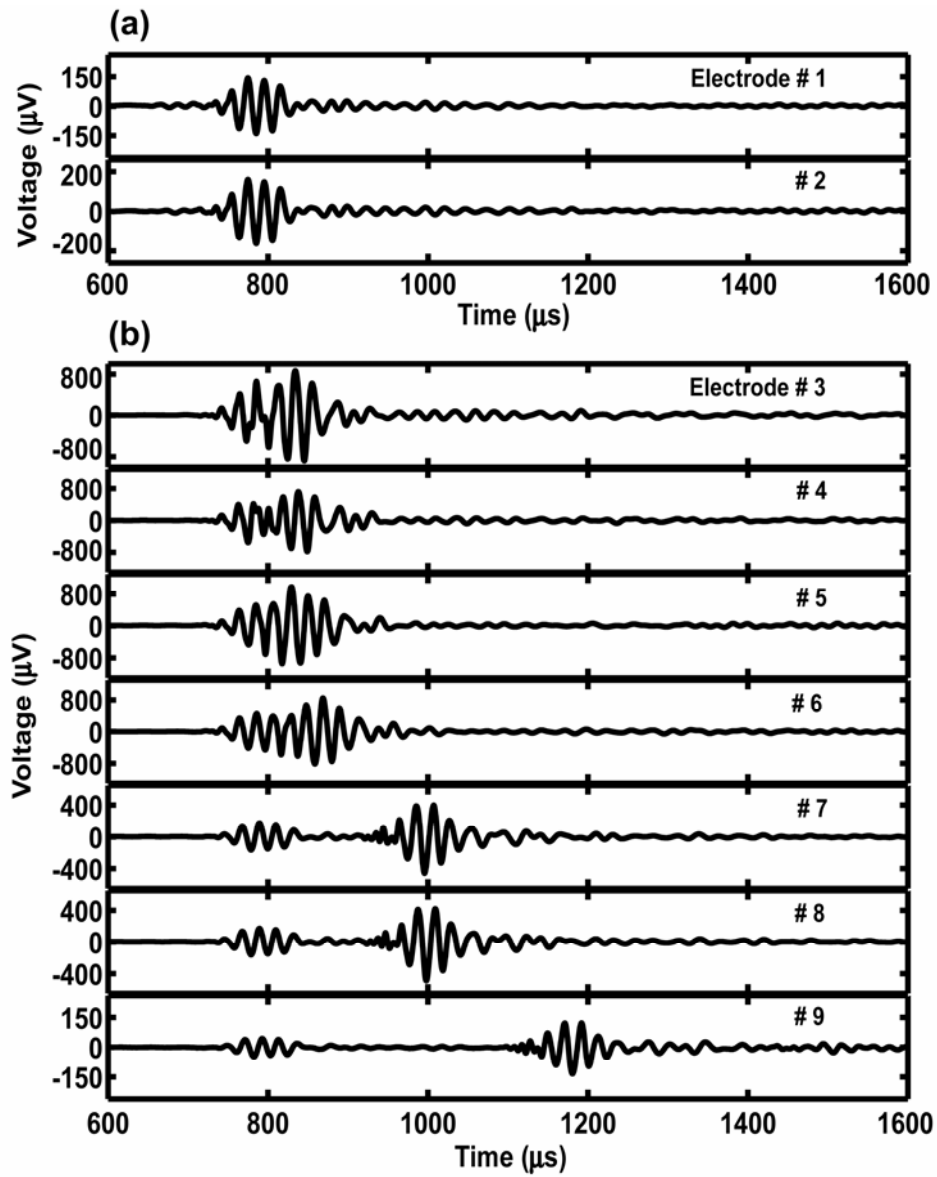


Figure 3

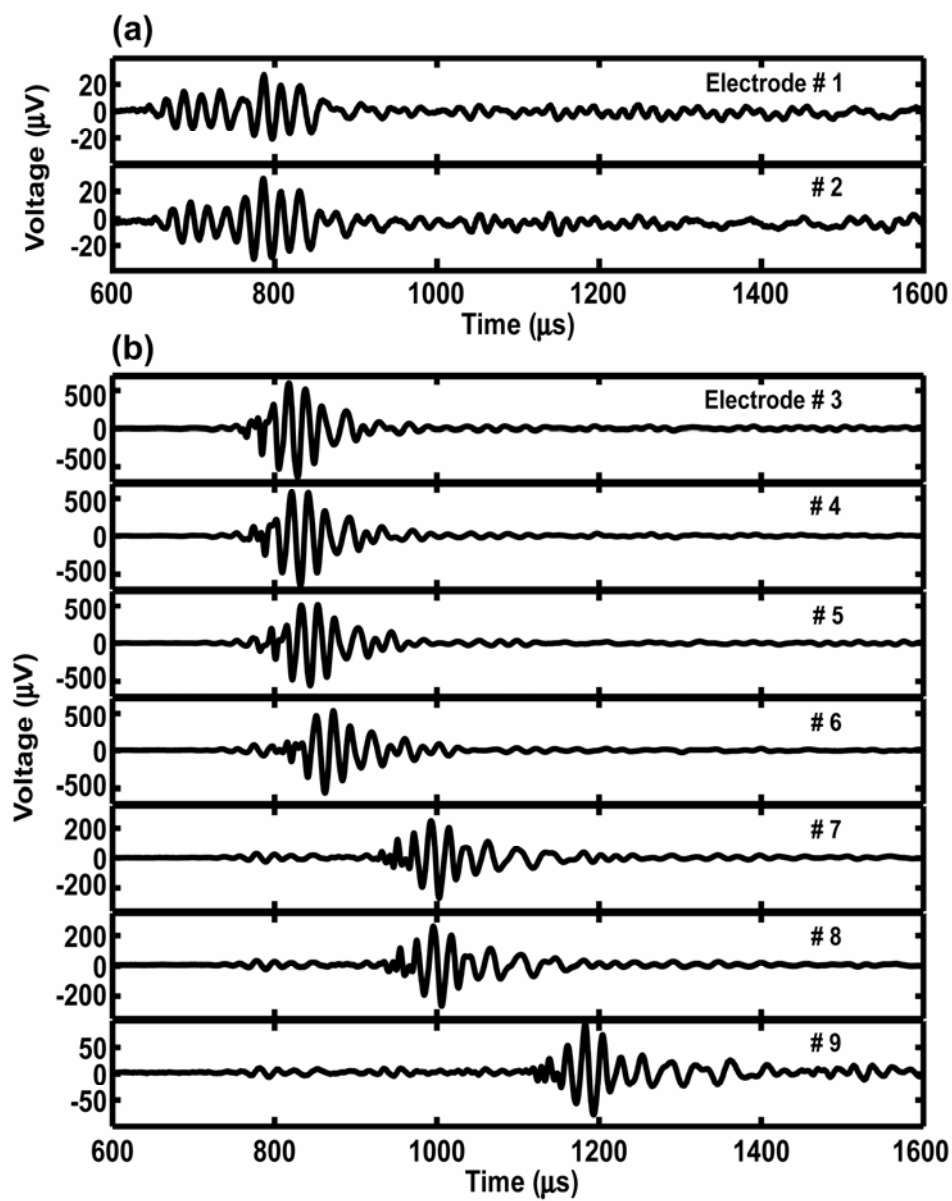


Figure 4

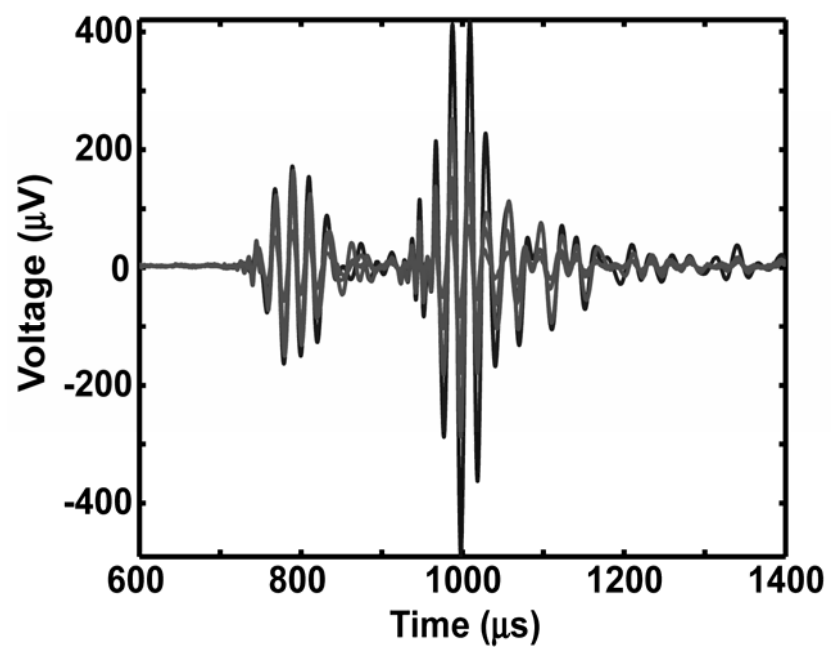


Figure 5

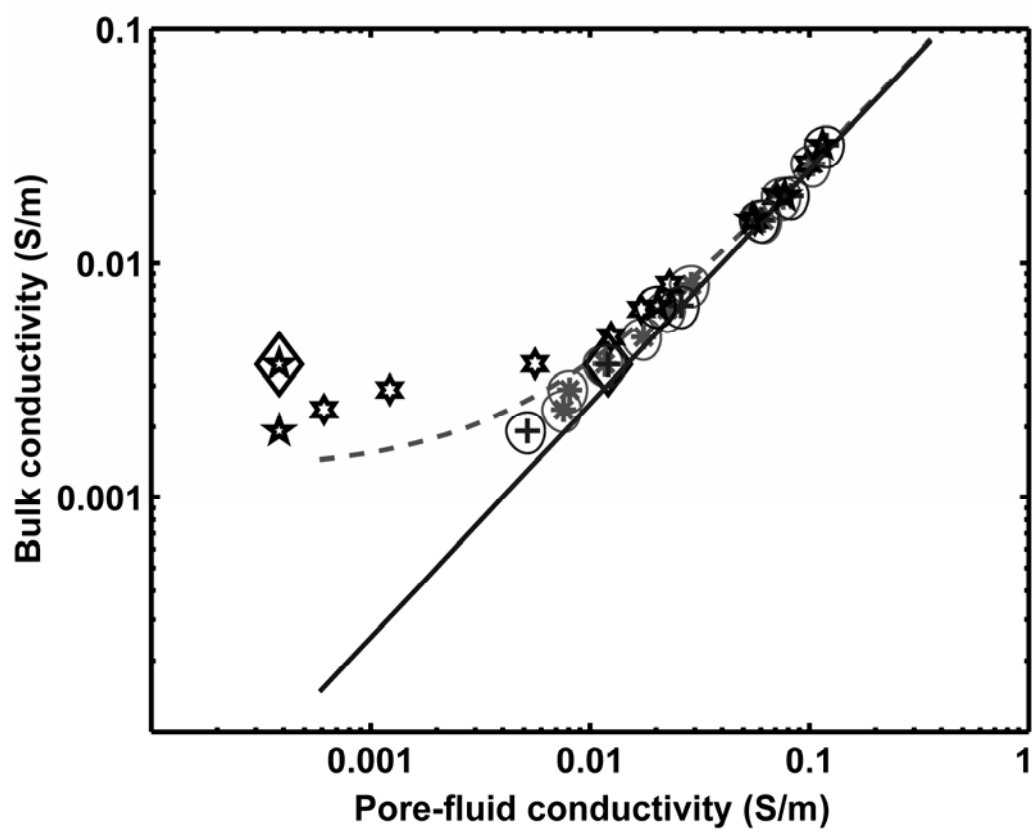


Figure 6

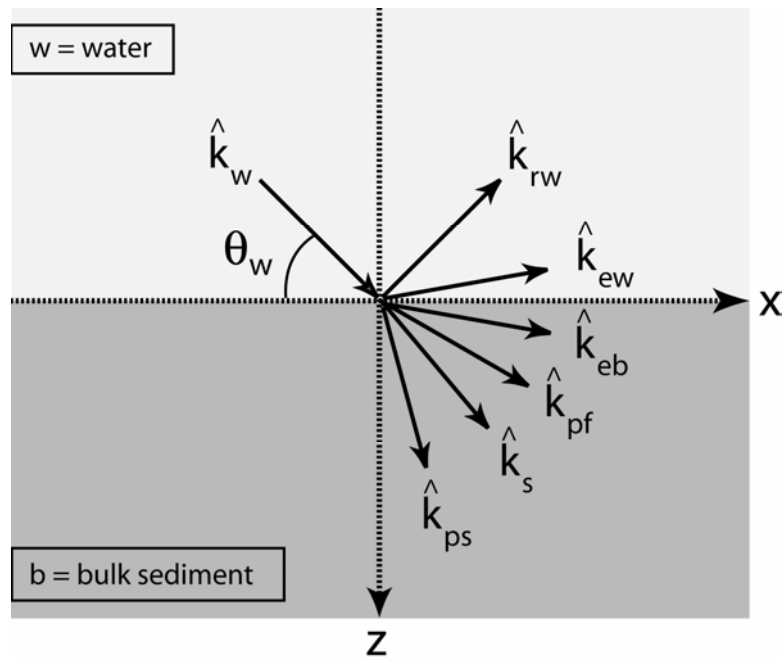


Figure 7

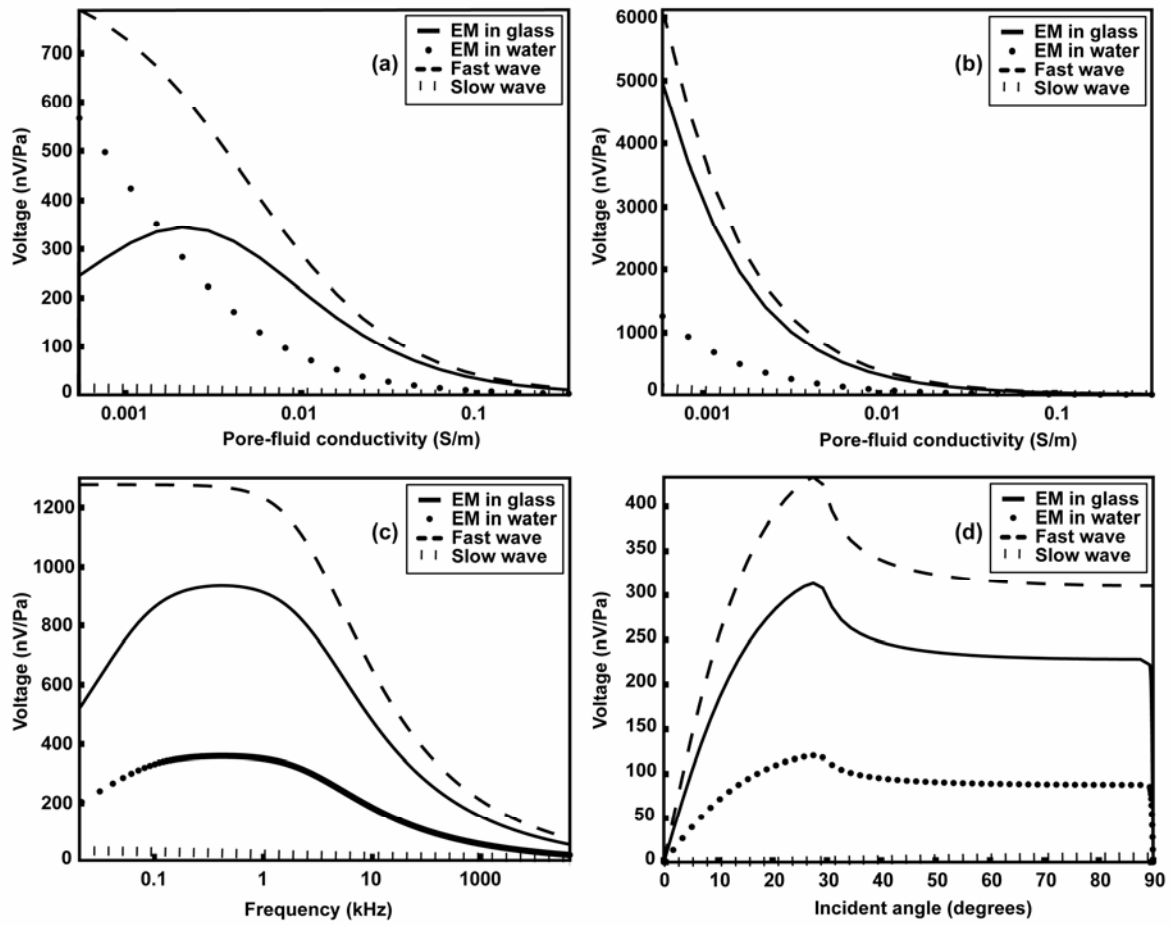


Figure 8

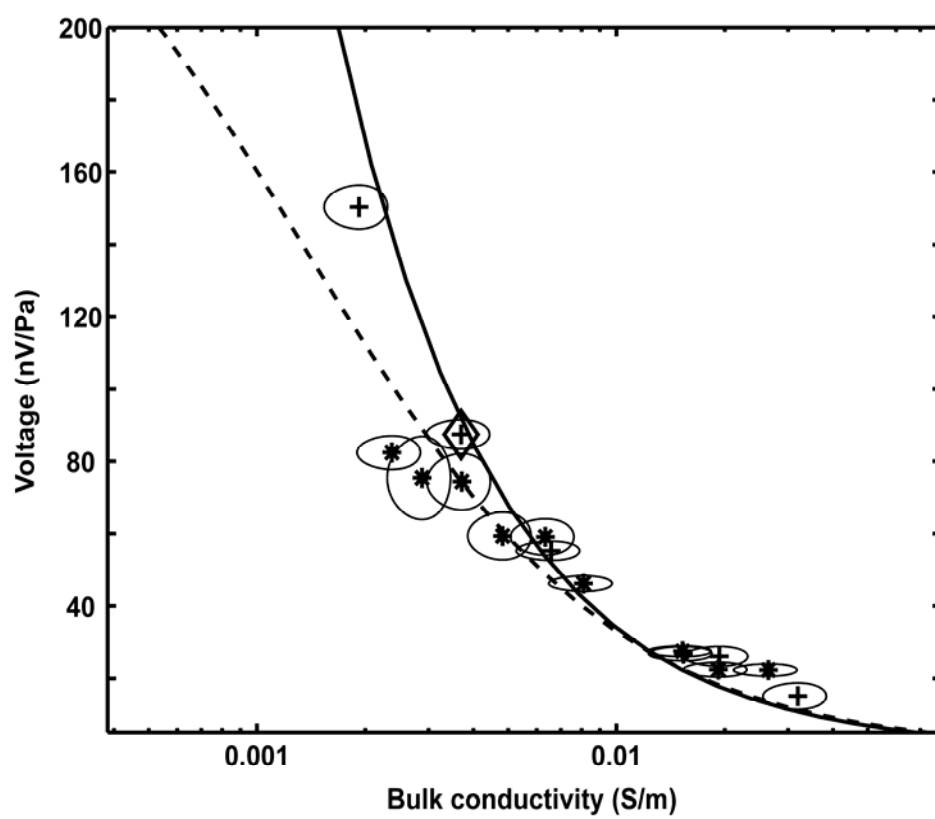


Figure 9